Research paper

Non-linear turbine selection for an OWC wave energy converter

I. López [a], R. Carballo [a,*], D.M. Fouz [a], G. Iglesias [b,c]

[a] *Área de Ingeniería Hidráulica, EPSE, Campus Terra, Universidade de Santiago de Compostela, 27002, Lugo, Spain*
[b] *School of Engineering and Architecture & MaREI, Environmental Research Institute, University College Cork, College Road, P43 C573, Cork, Ireland*
[c] *School of Engineering, Computing and Mathematics, University of Plymouth, Marine Building, Drake Circus, PL4 8AA, Plymouth, UK*

ARTICLE INFO

ABSTRACT

Turbine-induced damping is a critical parameter affecting the performance of oscillating water column (OWC) wave energy converters. Therefore, selecting the appropriate turbine-chamber combination is an essential step in their design. In this work, a methodology is developed to determine the optimum turbine diameter for a given chamber, i.e., the diameter which maximizes the pneumatic energy capture of the chamber under an extensive set of wave conditions—covering virtually the entire range of wave conditions relevant for wave energy exploitation. This novel approach combines physical and numerical modelling with dimensional analysis. Importantly, it results in a turbine diameter that enables the turbine to operate at maximum efficiency. Through the different modelling techniques applied, the methodology accounts for air compressibility effects and other non-linear effects. It is applicable to non-linear turbines, with the study focusing on the promising biradial turbine. The results indicate that using the proposed methodology to select the turbine diameter significantly improves the capture-width ratio of the OWC, with increases of up to 100% for individual sea states. Two turbine diameters were identified as appropriate for the proposed OWC chamber design, 1.1 m for low-energy sites, and 1.4 m for mid- and high-energy sites.

1. Introduction

With its vast untapped potential worldwide (Martinez and Iglesias, 2020), wave energy has a significant role to play in the energy transition. Wave energy can be exploited alone or in combination with wind energy (Astariz and Iglesias, 2016, 2017; Michele et al., 2019)—a promising option, which can be realised through hybrid systems mounted on shared substructures (Perez-Collazo et al., 2018, 2019; Pérez-Collazo et al., 2023) or through co-located farms consisting of structurally independent offshore wind turbines and WECs (Astariz et al., 2016). Research is under way on new hybrid wave energy systems (Bao et al., 2023; Chen and Wu, 2024; Cui et al., 2021), hybrid farms (Zheng et al., 2020b) and, more generally, novel wave energy converters (Lamont-Kane et al., 2024; López et al., 2018; Zheng et al., 2020c).

Among the variety of wave energy converters (WECs), oscillating water column (OWC) WECs are one of the most established (Falcão and Henriques, 2016) and present significant advantages. They lend themselves to integration with offshore wind turbines (Li et al., 2022; Liu et al., 2024; Veigas and Iglesias, 2015). In addition, multiple OWCs may be combined in a single platform (Zheng et al., 2020a; Zhou et al., 2021).

Another interesting possibility is their integration into coastal structures, such as breakwaters (Kim et al., 2022; Teixeira and Didier, 2023; Zheng et al., 2019). OWCs consist of a chamber partially filled with seawater and open below the water surface, along with an air turbine. The air inside the chamber is alternately compressed and decompressed by wave action, originating an alternate air flow through the turbine duct that propels the turbine and, consequently, the electric generator. The most common alternatives to take advantage of bidirectional air flow are the Wells and self-rectifying impulse turbines (Falcão et al., 2018). The Wells turbine (Raghunathan, 1995) is traditionally used in OWC wave energy converters, although it is currently undergoing new developments (Kotb et al., 2023). It is a reaction turbine that presents a high peak efficiency but a narrow operating range, being its behaviour approximately linear. Impulse turbines, both axial-flow (Luo et al., 2019) and radial-flow (Pereiras et al., 2011), present a comparatively wider operating range, but a lower peak efficiency. Over the last few years, a novel concept of self-rectifying impulse turbine, named biradial turbine, has emerged (Falcão et al., 2013). The biradial turbine presents a design in which both the inlet and the outlet face the radial direction, with centripetal inlet flow and centrifugal outlet flow. Importantly, the

---

* Corresponding author.
E-mail address: rodrigo.carballo@usc.es (R. Carballo).

biradial turbine merges the best of both Wells and impulse turbines, i.e., a high peak efficiency and a wide operating range (Falcão et al., 2018). Its reliability and performance have been demonstrated in sea trials at the Mutriku wave power plant (Gato et al., 2022).

In addition to the characteristics of the turbine, various factors related to the chamber affect the hydrodynamics and efficiency of an OWC device. These factors include the geometrical configuration of the entrance (Boccotti, 2007; Rezanejad et al., 2013), the slope of the chamber walls (Gaspar et al., 2020), the height of the underwater opening (Çelik and Altunkaynak, 2018, 2020) or the thickness and immersion depth of the front wall (Morris-Thomas et al., 2007). Among the parameters affecting the performance of an OWC device operating under a given wave climate, in addition to the characteristics of the turbine and chamber themselves, the coupling between these two elements, turbine and chamber, is of paramount importance (Çelik and Altunkaynak, 2019; López et al., 2015). The turbine induces a damping on the oscillations of the water column, thereby affecting the capture of pneumatic power (López et al., 2014). Simultaneously, this damping, which regulates the pressure versus flow rate relation achieved in the chamber, determines the operating conditions of the turbine, and hence its efficiency (Pereiras et al., 2015). Thus, selecting the most appropriate turbine for a given OWC chamber is a complex task due to the interplay of the hydrodynamics of the entire system. Matching the turbine to the chamber is, therefore, a common challenge in the development of an OWC power plant.

In previous works, a methodology has been developed to identify the value of the damping that maximizes the performance for a given OWC chamber at a particular costal location, that is, operating under a specific maritime climate (López et al., 2019). However, from a design perspective, it is more practical to provide a physical parameter of the turbine—such as the turbine diameter—rather than a value of the damping, which cannot be directly used for turbine design. Various approaches have been followed for matching the air turbine and the chamber in an OWC device. In most cases, stochastic methods based on linear wave theory were applied (Falcão, 2004). These methods, though, assume a linear behaviour of the turbine (a Wells turbine) or require linearization procedures that enable the turbine to be roughly modelled through a linear equation (Falcão et al., 2014). A non-linear methodology for matching a turbine to an OWC chamber was developed in (Pereiras et al., 2015) for axial and radial self-rectifying impulse turbines. Nevertheless, this approach considered only a limited number of regular wave conditions. Consequently, the motivation for this research arises from the lack of a straightforward method to determine the optimum turbine diameter for a non-linear turbine, particularly the biradial turbine, for a given OWC device operating under realistic irregular wave conditions while performing an accurate modelling which does not disregard important non-linear effects.

In this work, a procedure was developed to determine the best turbine-chamber combination for an OWC device operating under an extensive set of irregular wave conditions when equipped with a non-linear turbine, in particular, a biradial turbine. Thus, the objective was to identify, for a given chamber geometry, the biradial turbine diameter that enables the turbine to operate at its maximum performance, while maximizing the capture of wave energy of the chamber. To this end, a hybrid modelling methodology that combines physical and numerical modelling is proposed. Importantly, air compressibility effects, which are often disregarded albeit important in full-size OWC devices (López et al., 2020), were considered alongside other important non-linear effects, such as viscous losses. First, physical model tests were conducted under an extensive set of irregular wave conditions, considering four values of the turbine-induced damping, each representative of a specific turbine. These tests were complemented by computational fluid dynamics (CFD) numerical modelling, based on the Navier-Stokes equations for two compressible fluids. The numerical model plays an essential role in determining the pressure versus flowrate curves, enabling calculation of flowrate based on pressure drop measurements

from the physical model tests—measuring flowrate in wave flume experimental modelling is challenging. While numerical modelling was preferred in this case for its comprehensive analysis capabilities, alternative methods could also be considered. These include physical modelling in air tunnel (Sheng et al., 2014) or theoretical thermodynamic models (Medina-López et al., 2016, 2017; Sheng et al., 2013). Finally, dimensional analysis techniques were applied to develop a procedure for matching the turbine-induced damping to the turbine diameter which maximizes the turbine efficiency. By comparing the pneumatic energy capture of the different turbine diameters, that which performs better could be determined.

The structure of the paper is as follows. In Section 2, the physical modelling is presented, describing the OWC model, the experimental set-up, the testing campaign and the parameters evaluated. In Section 3, the numerical modelling is thoroughly depicted, including its validation against experimental data and the results obtained. In Section 4, the turbine dimensioning procedure is presented, along with its theorical basis. In Section 5, the impact of turbine diameter on the OWC performance is evaluated. Finally, the conclusions of the study are drawn in Section 6.

2. Physical modelling

2.1. OWC model

The OWC model represents at 1:30 scale the geometry designed in previous works (López et al., 2021) (Fig. 1). It extends across the entire width of the flume, being divided into three equal chambers, each measuring 0.186 m in width. The subsequent results pertain specifically to the middle chamber. The geometry of the model is based on the L-shaped OWC design, in which a horizontal duct is added to the chamber to increase the resonant frequency of the system (Howe and Nader, 2017; Rezanejad et al., 2019). The dimensions of the device were appropriately tunned in order to achieve near-resonant conditions when operating under the sea states with the highest energy at the site of interest. In particular, the aim was to achieve near-resonant conditions for periods around 9–10 s at low to moderate water depths.

The wet part of the model was scaled to ensure that Froude number is equal between the model and prototype. This is necessary when dealing with free surface flows (Hughes, 1993). In addition, to correctly reproduce air compressibility effects—a significant effect in full-size OWC converters (Falcão and Henriques, 2019)—the approach proposed in (Falcão and Henriques, 2014) was followed. According to this approach, the ratio of model to prototype air chamber volume must follow:

$$\frac{V_p}{V_m} = n_p \, \lambda^2 \, \delta, \tag{1}$$

where V represents the volume of the air chamber; n_p is the polytropic exponent of the turbine; λ is the scale factor (in this case 30); δ is the ratio of model to prototype water density, and the subscripts m and p refer to the model and prototype, respectively. An alternative approach, based on the isentropic assumption, and hence most appropriate for representing the exhalation phase, is proposed in Falcão and Henriques (2019).

According to Eq. (1) and considering a water density ratio $\delta = 0.98$ and a polytropic exponent of the turbine $n_p = 1.2$ (Falcão and Henriques, 2014), the volume of the air chamber at model dimensions must be $V_m = 267.9$ dm³. To achieve this air volume, a practical solution is to connect the air chamber of the model to a rigid-walled air reservoir partially filled with water to adjust the air volume to the desired value. Given that the air chamber of the model (Fig. 1), scaled assuming perfect geometrical similarity, has a volume of 10.5 dm³ and the connection pipe between the model and the air reservoir adds another 19.4 dm³, an additional air volume of 238 dm³ was provided through the reservoir.

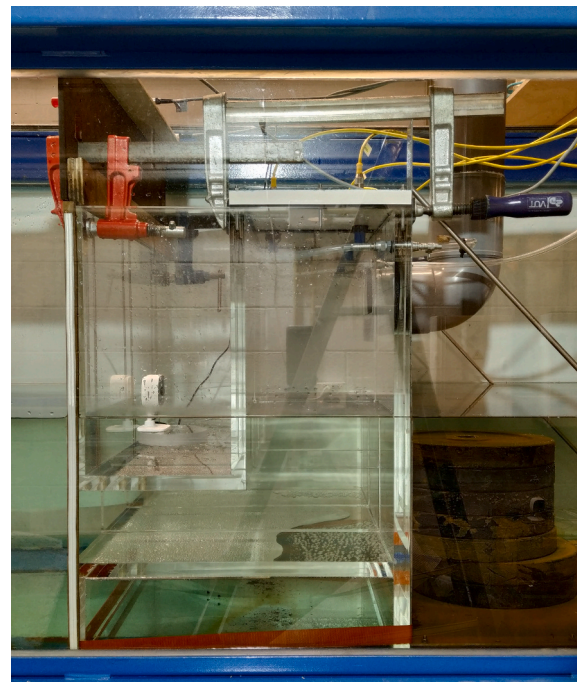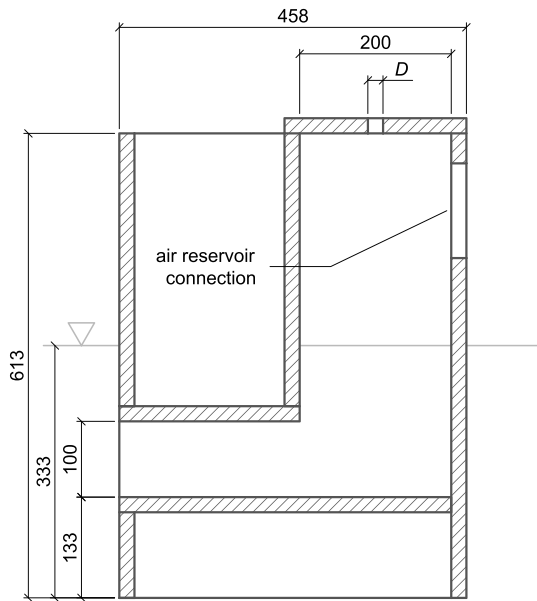The impact of the turbine on the system was simulated using an

Fig. 1. Cross-section of the OWC physical model at 1:30 scale (dimensions in mm) (left) and photograph of the model set up in the wave flume (right).

orifice, which replicates the quadratic relation between the pressure drop and the air flow rate in impulse turbines (Falcão and Gato, 2012). This is a well-established method for emulating the turbine-induced damping of non-linear turbines, as demonstrated in previous studies (Falcão and Henriques, 2014). Four different orifice diameters were tested: $d = 17, 22, 25$ and 29 mm, corresponding to orifice ratios (orifice area over cross-sectional plan area of the model air chamber) of 0.6%, 1.0%, 1.3% and 1.8%, respectively.

2.2. Experimental set-up

Tests were conducted at the Hydraulic Laboratory of the University of Santiago de Compostela, provided with a wave flume that is 20 m long, 0.65 m wide, and has a height of 0.95 m. The wave generation system consists of a piston-type paddle equipped with an active wave absorption system to prevent re-reflections. The experimental set-up is presented in Fig. 2. The instrumentation used encompassed nine wave gauges to measure the free surface elevations at different positions, two ultrasonic level sensors to monitor water column oscillations, and a differential pressure transducer to record the difference in pressure between the atmosphere and the interior of the chamber.

The experimental campaign consists of two sets of tests. The first one, which comprises 15 regular wave conditions, aims to validate the

Table 1
Regular wave conditions tested in the experimental campaign.

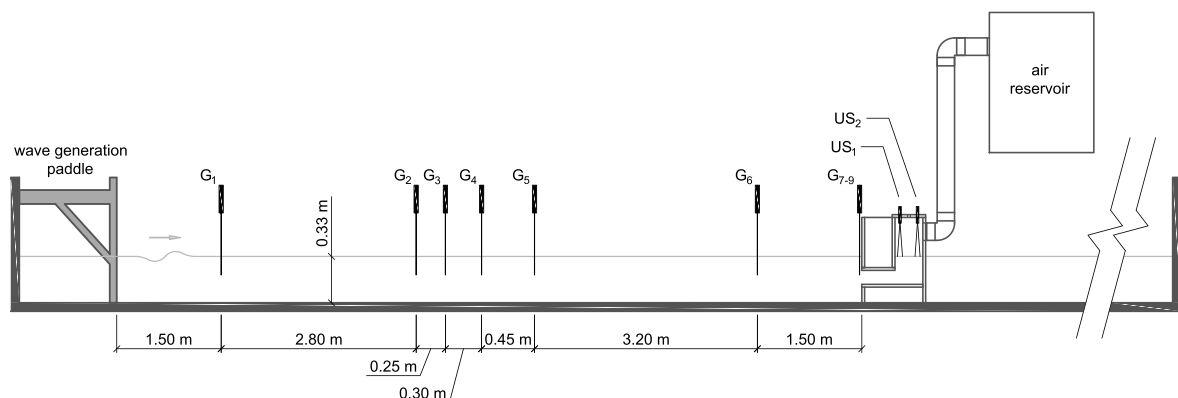| Test	Prototype dimensions		Model dimensions	
	H (m)	T (s)	H (m)	T (s)
1	1.0	7	0.033	1.28
2	1.0	8	0.033	1.46
3	1.5	8	0.050	1.46
4	2.0	8	0.067	1.46
5	1.0	9	0.033	1.64
6	1.5	9	0.050	1.64
7	2.0	9	0.067	1.64
8	2.5	9	0.083	1.64
9	3.0	9	0.100	1.64
10	1.5	10	0.050	1.83
11	2.0	10	0.067	1.83
12	2.5	10	0.083	1.83
13	3.0	10	0.100	1.83
14	2.5	11	0.083	2.01
15	3.0	11	0.100	2.01

Fig. 2. Experimental set-up.

numerical model (Table 1). The second set comprises 42 irregular wave conditions, each representing a specific *energy bin* (Fig. 3). These energy bins are bivariate intervals which discretize the sea states based on their significant wave height (H_{m0}) and energy period (T_e) (Carballo and Iglesias, 2012). An interval size of $\Delta H_{m0} = 1$ m and $\Delta T_e = 1$ s was used. A JONSWAP spectrum (Hasselmann et al., 1980) was assumed for testing each of the representative wave conditions. A total of 228 tests were carried out, taking into account the regular and irregular wave conditions, as well as the different orifice diameters tested.

2.3. Performance evaluation

The mean pneumatic power captured by the OWC converter was computed following:

$$P_p = \frac{1}{t_{max}} \int_0^{t_{max}} \Delta p \, Q \, dt, \tag{2}$$

where Δp is pressure drop; Q is air flow rate; and t_{max} is the total duration of the test. First, the ratio $\Delta p \, Q^{-2}$ of each orifice diameter was obtained from numerical modelling (see Section 3). Once these ratios were known, they were used to obtain the flow rate through the orifice from the pressure drop measurements in the experimental campaign.

The mean wave power for each test was calculated as:

$$P_w = \rho_w g \int_0^\infty S(f) C_g(f) \, df, \tag{3}$$

where ρ_w represents the density of water; $S(f)$ is the spectral energy density obtained from an incident-reflected wave analysis; and C_g is the group velocity of each frequency band.

The capture-width ratio was computed as:

$$C_{WR} = \frac{P_p}{P_w w_c} \tag{4}$$

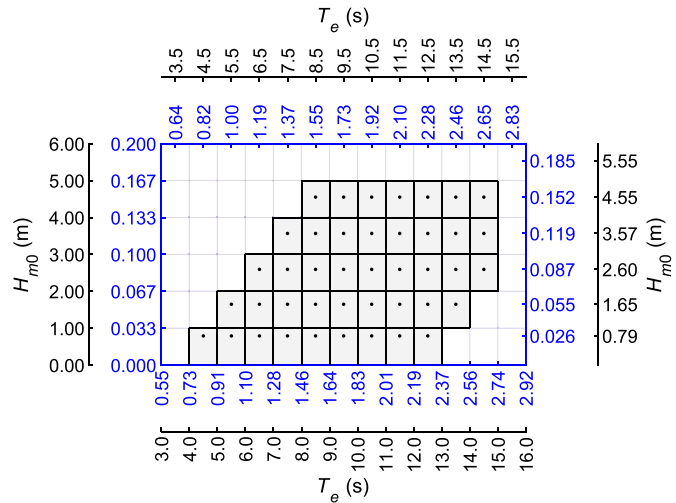where w_c is the air chamber width (in direction parallel to wave fronts).

Fig. 3. Irregular wave conditions tested in the experimental campaign, in prototype dimensions (in black) and model dimensions (in blue). The left and bottom axes indicate the boundaries of the energy bins and the top and right axes the representative conditions of each bin.

3. Numerical modelling

3.1. Governing equations

The *compressibleInterFoam* multiphase solver, which is a finite-volume-based solver integrated into the OpenFOAM package, was used to solve the wave-WEC interaction while considering air compressibility effects. The governing equations of the solver are the continuity (5), momentum (6), and energy (7) equations:

$$\frac{\partial \rho}{\partial t} + \nabla \bullet (\rho \boldsymbol{U}) = 0, \tag{5}$$

$$\frac{\partial (\rho \boldsymbol{U})}{\partial t} + \nabla \bullet (\rho \boldsymbol{U}\boldsymbol{U}) = -\nabla p + \nabla \bullet \boldsymbol{\tau} + \rho \boldsymbol{g} + \boldsymbol{f_{ST}}, \tag{6}$$

$$\frac{\partial (\rho T_K)}{\partial t} + \nabla \bullet (\rho T_K \boldsymbol{U}) - \nabla \bullet (\alpha_{\text{eff}} \nabla T_K) = -\left(\frac{\gamma}{c_{v,\text{liquid}}} + \frac{1-\gamma}{c_{v,\text{gas}}} \right)\left(\nabla \bullet (p\boldsymbol{U}) + \frac{\partial (\rho K)}{\partial t} + \nabla \bullet (\rho K \boldsymbol{U}) \right), \tag{7}$$

where ρ is the density of the mixture of the two phases; $\boldsymbol{U}$ is the velocity vector; t is time; p is pressure; $\boldsymbol{\tau}$ is the viscous stress tensor; $\boldsymbol{g}$ is the gravity vector; $\boldsymbol{f_{ST}}$ is the surface tension force; T_K is the temperature; α_{eff} is a phase-averaged thermal diffusivity; $c_{v,\text{liquid}}$ and $c_{v,\text{gas}}$ are the specific isochoric heat capacities of the liquid and the gas phases, respectively; K is the kinetic energy per unit mass; and γ is the volume-of-fluid (VOF) phase-fraction function (Hirt and Nichols, 1981), which represents the liquid fraction in each cell, and enables the tracking of the interface between the two phases. Thus, both fluids are jointly considered as a mixture whose properties vary in space according to the volume fraction of each phase, e.g.:

$$\rho = \gamma \rho_{liquid} + (1 - \gamma)\rho_{gas} . \tag{8}$$

The ideal gas equation was used to model the air compressibility:

$$\rho_{gas} = \frac{p}{R_S T_K}, \tag{9}$$

where R_S is the specific gas constant. The water was considered as an incompressible fluid, i.e., ρ_{liquid} is constant.

For the closure of the equations, a turbulence model that enables the calculation of the viscous stress tensor is needed. The k-ω-SST model (Menter et al., 2003) for compressible flows was used. Finally, wave generation was implemented using the *waves2Foam* toolbox (Jacobsen et al., 2012), which employs the relaxation zone technique to create (and absorb) waves. The relaxation zone is a numerical approach that forms part of the internal wave generation methods, in which waves are generated within a region defined inside the computational domain. Furthermore, the relaxation zone enables passive wave absorption for dealing with reflected waves and avoiding re-reflections into the domain. The method modifies the volume fraction and velocity fields by blending a target solution with the computed solution:

$$\phi = (1 - \omega_R) \, \phi_{target} + \omega_R \, \phi_{computed}, \tag{10}$$

where ϕ is either $\boldsymbol{U}$ or γ; and ω_R is the relaxation function, an exponential weighting function which varies along the relaxation zone, taking on a value of unity at the interface between the relaxation zone and the propagation zone (see numerical set-up below) and a value of zero at the boundary of the computational domain. The relaxation zone was originally implemented for the incompressible *interFoam* solver but has been applied in this work to the compressible version, *compressibleInterFoam*, by modifying its source code.

3.2. Computational domain

Fig. 4 presents the computational domain, which mirrors the
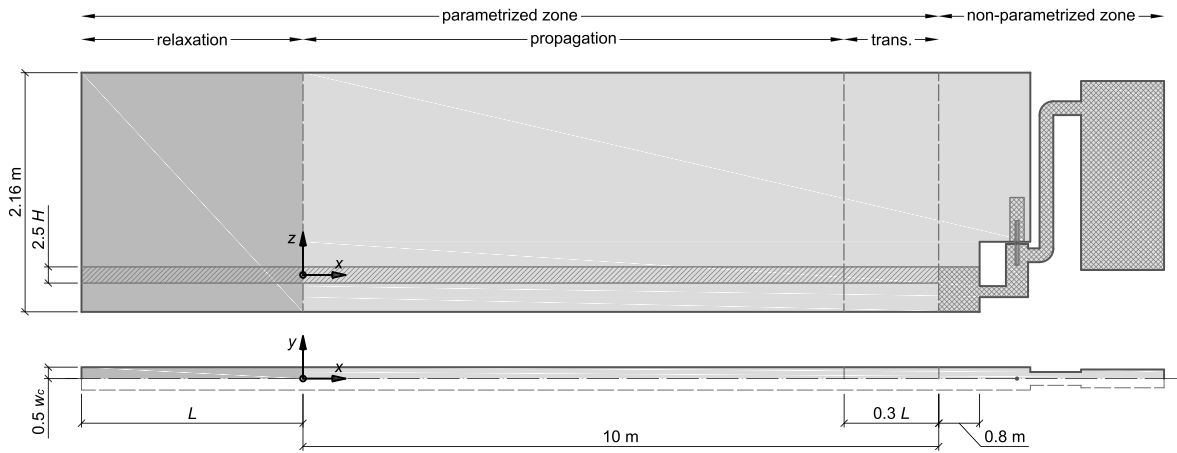
Fig. 4. Numerical set-up.

experimental shown in Fig. 2. It constitutes a 3D model that includes the OWC device, the air reservoir and the connection between both elements, with the addition of an extra upstream section for implementing the internal wave generation and absorption method. The air reservoir is dimensioned to provide the same air volume as in the experimental model while its width is adjusted to match that of the chamber. By resorting to a symmetry boundary condition, only half chamber is considered.

Hexahedral elements were used to discretize the computational domain using the *blockMesh* and *snappyHexMesh* utilities from the OpenFOAM package (Fig. 5). The mesh can be divided into two main regions based on whether it is parametrized according to the wave conditions or not: (i) the parametrized flume region; and (ii) the unparametrized model-testing region. The parametrized mesh ensures an optimal mesh configuration for propagating waves, irrespective of the generated wave conditions. However, in the zone of the domain where the mesh has to be adapted to the model geometry, it is preferable to have an orthogonal mesh consisting of squared hexahedra, which is achieved by creating the non-parametrized region. The combinations of these two approaches ensures optimal conditions for both wave propagation and the meshing of the model, regardless of the testing conditions.

The flume region comprises the relaxation zone, the propagation zone, and a transition zone in which the cell size is gradually adjusted
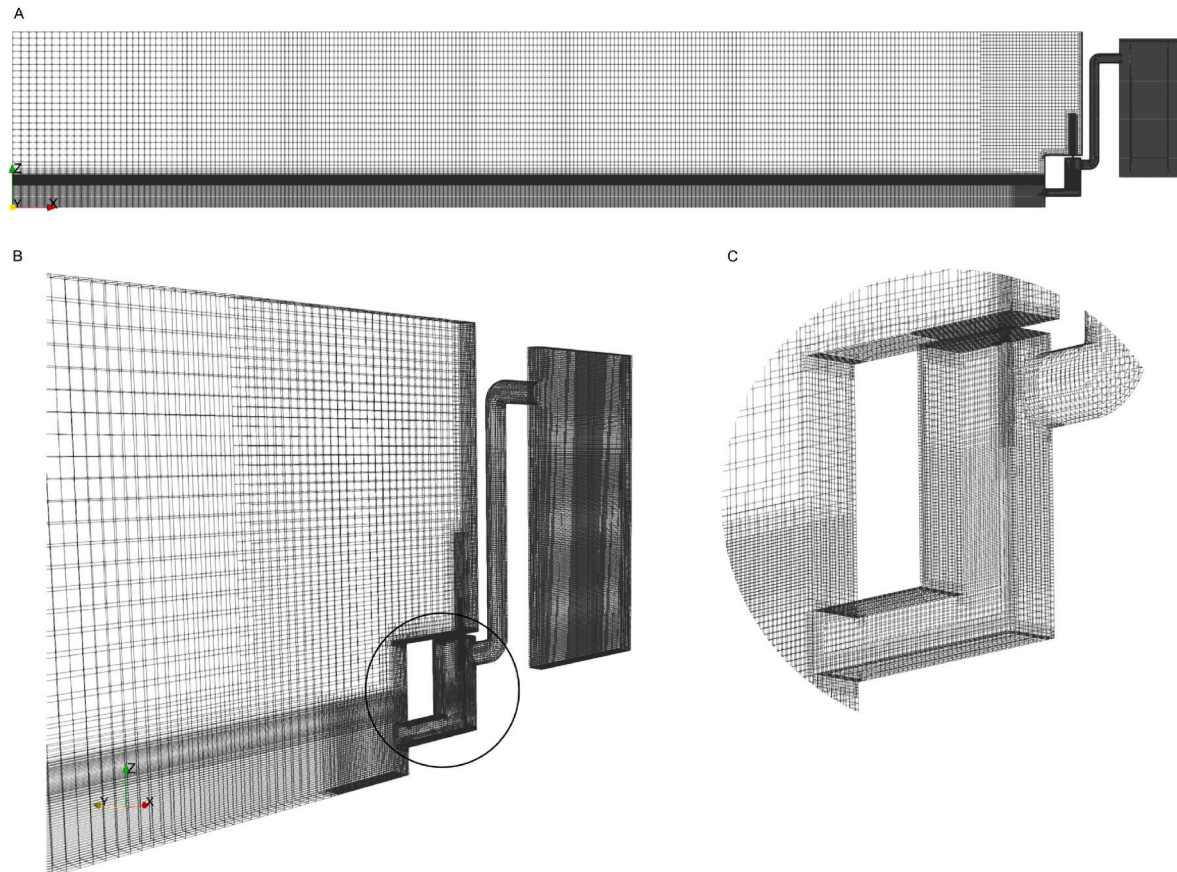

Fig. 5. Numerical mesh: (A) side view of the whole mesh domain; (B) 3D view of the non-parametrized zone; and (C) detail of the OWC mesh.

from the propagation zone to the model-testing region. A uniform mesh was defined along the *x*-direction in this region (Fig. 5) with a cell size that ensures 50 cells per wavelength, as recommended by (Vanneste and Troch, 2015). On the contrary, a non-uniform mesh was used in the *z*-direction, with a finer grid around the free surface (López et al., 2014). The cell size in the *z*-direction was established to ensure that, at least, there exist 8 cells per wave height (Simonetti et al., 2018). The number of cells in *y*-direction was limited to 4, given that no 3D effects are expected in this region. As can be seen in Fig. 4, lengths of one wavelength and one-third of the wavelength were used for the relaxation zone and the transition zone, respectively.

As previously mentioned, the model-testing region consists of an unparametrized mesh with a base cell size of $\Delta x = \Delta y = \Delta z = 0.04$ m, resulting in a mesh with an aspect ratio of one. The mesh around the OWC model was refined by using up to four refinement levels (in each refinement the cells are halved) and subsequently morphed to fit the geometry of the OWC model. A minimum cell size of 2.5×10^{-3} m was used. The boundary conditions are summarized in Table 2. The final mesh contained approximately half a million cells. The computations were performed on an Intel Xeon E5-2680 V3 processor. Each case was executed in parallel, utilizing 6 cores; the computation for a single case required approximately 4 days to complete.

Assuming the pressure versus flow rate relationship for each orifice diameter is nearly constant, i.e., it does not depend on the wave conditions (López et al., 2020), a sample of four wave conditions were simulated: $H = 0.033$ m, $T = 1.46$ s; $H = 0.050$ m, $T = 1.64$ s; $H = 0.067$ m, $T = 1.83$ s; and $H = 0.083$ m, $T = 2.01$ s. To validate the numerical model, both the water column oscillations (at the same positions where the two ultrasonic level sensors were located in the experimental tests) and the differential air pressure were obtained. Furthermore, the air flow rate through each orifice was computed to calculate the ratio of pressure drop to air flow rate.

3.3. Numerical model validation

The validation of the numerical model was carried out by comparing the oscillations of the water column and the pressure drop time series with the numerical model data. The goodness-of-fit was evaluated based on the coefficient of determination (R^2) and the normalised root mean square error (NRMSE) (Table 3). In general, the agreement found is very good, with average values of the NMRSE below 5% for the free surface elevations and around 6% in the case of the pressure drop. The coefficient of determination presents values well above 0.90 for the three variables.

For illustration, the time series from experimental and numerical models are presented in Figures Figs. 6 and 7. It can be seen that both the

Table 2
Summary of the boundary conditions applied to the different fields (wavefunction: waves2Foam wave generating functions; wall-function: special wall functions for the turbulence model; inlet-outlet-vel: zero-gradient for outflow, calculated value for inflow; inlet-outlet: zero-gradient for outflow, fixed value for inflow).

	phase-fraction	pressure	velocity	temperature	k/ω
inlet	wave-function	calculated	wave-function	zero-gradient	zero-gradient
outlet	zero-gradient	calculated	no-slip	zero-gradient	zero-gradient
top	inlet-outlet	calculated	inlet-outlet-vel	inlet-outlet	inlet-outlet
bottom	zero-gradient	calculated	no-slip	zero-gradient	wall-function
front	symmetry	symmetry	symmetry	symmetry	symmetry
back	symmetry	symmetry	symmetry	symmetry	symmetry
model	zero-gradient	calculated	no-slip	zero-gradient	wall-function

amplitude and period of the different time series are accurately reproduced by the numerical model. In fact, even in the case when the oscillations of the water column do not follow a piston-like motion (i.e., the amplitude of the oscillations at the front and rear positions are not the same), the agreement is very good (e.g., Fig. 6, top and mid panels). Furthermore, the results are consistent for the different orifice diameters that were tested.

3.4. Pressure drop versus air flow rate ratios

Fig. 8 shows the pressure versus air flow rate data points obtained from the numerical model simulations are represented for the four orifice diameters. The ratio $\Delta p \, Q^{-2}$ of each orifice diameter was obtained by fitting a parabola to the data points of each orifice, following the procedure described in (López et al., 2020). The pressure versus flow rate ratios were determined for the orifice diameters tested $d = 17$, 22, 25 and 29 mm, resulting in values of 2.1×10^7, 7.5×10^6, 4.6×10^6 and 2.6×10^6 kg m^7, respectively. Once these ratios were known, they were used to obtain the flow rate in the experimental campaign, from the pressure drop measurements.

4. Turbine dimensioning

4.1. Dimensional analysis of the chamber

The flow rate through the turbine of an OWC wave energy converter (Q) can be expressed as a function of the pressure drop between the interior of the chamber and the atmosphere (Δp), the wave height (H), the wave period (T), the gravitational acceleration (g), the water density (ρ_w) and the characteristic length of the device (L) (e.g., the diameter in the case of an axisymmetric device):

$$Q = f_Q(\Delta p, H, T, g, \rho_w, L) . \tag{11}$$

The surface tension and viscosity forces are ignored in the analysis because, as stated above, in free surface flows they are of comparatively much less importance than the inertia forces (Hughes, 1993). Applying Buckingham Pi theorem, the following dimensionless products are obtained:

$$\Pi_1 = \frac{Q}{L^{5/2} g^{1/2}} , \tag{12}$$

$$\Pi_2 = \frac{\Delta p}{L \, \rho_w \, g} , \tag{13}$$

$$\Pi_3 = \frac{H}{L} , \tag{14}$$

$$\Pi_4 = \frac{L^{1/2}}{T \, g^{1/2}} . \tag{15}$$

Thus, Eq. (10) can be rearranged in dimensionless form as:

$$\frac{Q}{L^{5/2} g^{1/2}} = f_{\Pi_1} \left(\frac{\Delta p}{L \, \rho_w \, g}, \frac{H}{L}, \frac{L^{1/2}}{T \, g^{1/2}} \right) . \tag{16}$$

where the last dimensionless product of the right-hand side of the equation is the Froude number.

The combination of the dimensionless products Π_1 and Π_2 yields the dimensionless damping coefficient of the chamber:

$$B_c = \frac{\Delta p^{1/2}}{Q} \frac{A_c}{\rho_w^{1/2}} . \tag{17}$$

where A_c is the cross-sectional plan area of the air chamber, chosen to better represent the geometry of rectangular-shaped chambers. The dimensionless damping coefficient of the chamber represents the turbine-induced damping, i.e., the attenuation that the turbine exerts on

Table 3

Values of the coefficient of determination (R^2) and the normalised root-mean-square error (NRMSE) for the numerical model validation tests. The wave conditions are presented in Table 1. The subscripts refer to pressure drop (Δp) and free surface elevation at ultrasonic level sensor 1 and 2 (US1 and US2, respectively).

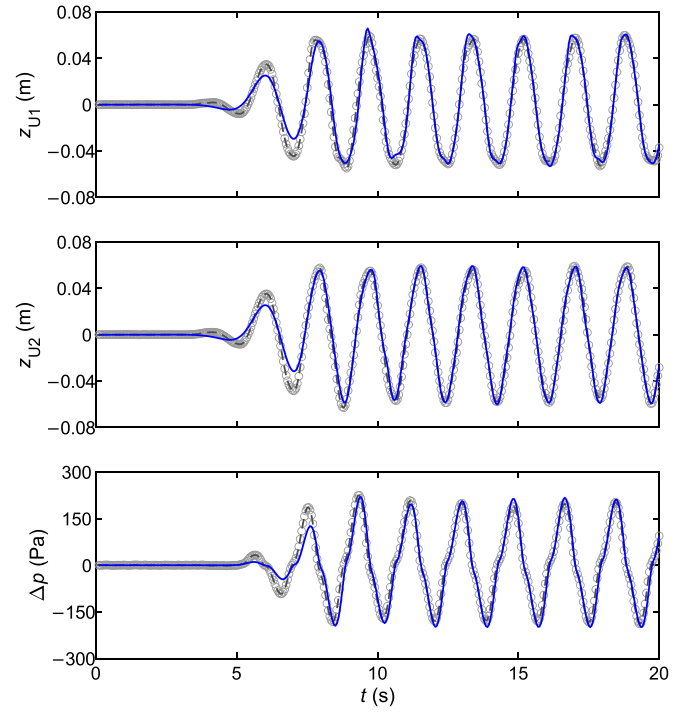| Wave condition	Orifice diameter (mm)	$R^2_{\Delta p}$	NRMSE$_{\Delta p}$	R^2_{US1}	NRMSE$_{US1}$	R^2_{US2}	NRMSE$_{US2}$
02	17	0.94	7.18%	0.97	5.69%	0.98	5.02%
06	17	0.96	5.97%	0.97	5.79%	0.97	5.83%
11	17	0.95	7.13%	0.97	5.07%	0.97	5.17%
14	17	0.94	8.97%	0.96	6.29%	0.97	5.17%
02	22	0.94	6.45%	0.98	5.30%	0.98	5.12%
06	22	0.96	5.54%	0.98	4.44%	0.98	4.87%
11	22	0.96	6.18%	0.98	3.98%	0.98	4.23%
14	22	0.96	6.90%	0.98	4.71%	0.98	3.64%
02	25	0.94	6.26%	0.97	5.03%	0.97	4.69%
06	25	0.97	5.16%	0.99	3.12%	0.99	3.42%
11	25	0.97	4.81%	0.98	3.94%	0.98	4.35%
14	25	0.97	6.59%	0.98	5.07%	0.98	3.89%
02	29	0.95	5.75%	0.97	5.21%	0.97	5.06%
06	29	0.96	5.04%	0.97	4.93%	0.97	5.37%
11	29	0.97	5.23%	0.98	3.89%	0.98	4.42%
14	29	0.97	5.66%	0.97	5.19%	0.98	4.08%
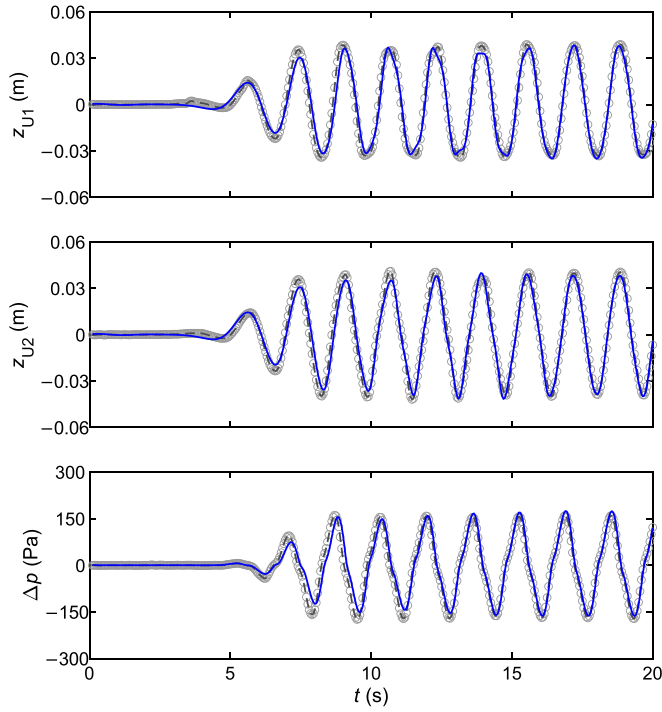
Fig. 6. Comparison of the oscillations of the water column at US1 (top panel) and US2 (mid panel) positions and pressure drop (bottom panel) from experiments and numerical model. The wave condition for this data is $H = 0.05$ m and $T = 1.64$ s, with an orifice diameter of $d = 22$ mm (– numerical model; ○ experimental measurements).

Fig. 7. Comparison of the oscillations of the water column at US1 (top panel) and US2 (mid panel) positions and pressure drop (bottom panel) from experiments and numerical model. The wave condition for this data is $H = 0.067$ m and $T = 1.83$ s, with an orifice diameter of $d = 25$ mm (– numerical model; ○ experimental measurements).

the water column oscillations. The values of B_c for the tested orifice diameters ($d = 17$, 22, 25 and 29 mm) are 5.4, 3.2, 2.5 and 1.9, respectively.

4.2. Dimensional analysis of the turbine

Assuming large values of the Reynolds number and ignoring Mach number effects, the dynamics of an air turbine are described in dimensionless form through the application of Buckingham Pi theorem as (Dick, 2015):

$$\Phi = f_\Phi(\Psi), \tag{18}$$

$$\Xi = f_\Xi(\Psi), \tag{19}$$

where Ψ is the dimensionless pressure head; Φ is the dimensionless flow rate; and Ξ is the dimensionless power coefficient, which are defined as:

$$\Psi = \frac{\Delta p}{\rho_a \Omega^2 D^2}, \tag{20}$$

$$\Phi = \frac{\dot{m}_{turb}}{\rho_a \Omega D^3}, \tag{21}$$

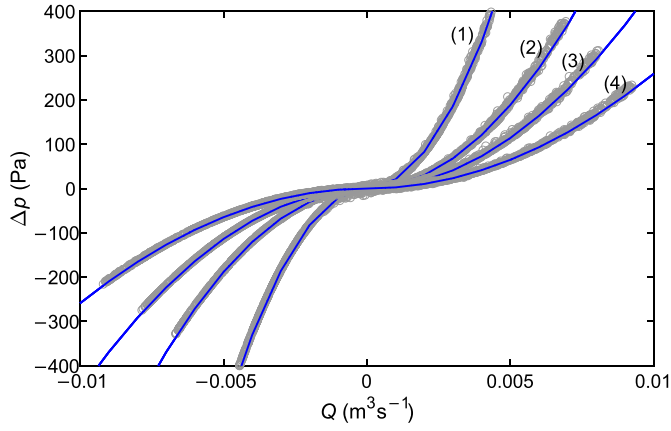$$\Xi = \frac{P_{turb}}{\rho_a \Omega^3 D^5}, \tag{22}$$

Fig. 8. Pressure drop versus air flow rate data points and fitted parabolic curves for the four tested orifice diameters: (1) $d = 17$ mm; (2) $d = 22$ mm; (3) $d = 25$ mm; and (4) $d = 29$ mm.

where Ω is the rotational speed of the turbine; D is the rotor diameter; $\dot{m}_{turb}$ is the mass flow rate of air through the turbine; and P_{turb} is the instantaneous turbine aerodynamic power.

Based on these coefficients the turbine efficiency is defined as:

$$\eta_{turb} = \frac{\Xi}{\Psi \, \Phi} \; . \tag{23}$$

Operating with the dimensionless flow rate (Φ) and dimensionless pressure head (Ψ) coefficients, the dimensionless damping coefficient of the turbine can be defined as:

$$B_t = \frac{\Phi}{\Psi^{1/2}} = \frac{Q}{\Delta p^{1/2}} \frac{\rho_a^{1/2}}{D^2} \; . \tag{24}$$

4.3. Calculation of turbine diameter

The optimum turbine diameter for a given chamber is that which enables the operation of the turbine at maximum performance and, at the same time, provides to the chamber the damping that maximizes the capture of wave energy. Combining Eqs. (16) and (23), the turbine diameter can be obtained as:

$$D = \left(\frac{A_c \, \rho_a^{1/2}}{B_t \, B_c \, \rho_w^{1/2}} \right)^{1/2} \; . \tag{25}$$

In Eq. (24), the dimensionless damping coefficient of the chamber (B_c) that maximizes the capture of wave energy can be determined from experimental modelling. In addition, the value of the dimensionless damping coefficient of the turbine (B_t) can be fixed to that corresponding to the best efficiency point ($B_{t,bep}$), i.e., the value of the dimensionless damping coefficient of the turbine under which the turbine operates at its maximum performance. The performance characteristics of a biradial turbine expressed in terms of the efficiency (η_{turb}) and the dimensionless flow rate (Φ) and power (Ξ) coefficients are presented in Fig. 9.

Based on Fig. 9, the dimensionless damping coefficient of the turbine (B_t) that corresponds to the best efficiency point is $B_t = B_{t,bep} = 0.186$. Thus, the biradial turbine that, for a given OWC chamber, provides a given value of the damping (B_c) while overall providing optimum performance, must have a diameter that follows Eq. (24), with $B_t = B_{t,bep} = 0.186$. For the case study presented in this work, the diameter of the full-size biradial turbines that correspond to the values of the dimensionless damping coefficient of the chamber (B_c) tested, considering a cross-sectional plan area of the full-size air chamber $A_c = 5.58 \times 6.0 = 33.48$ m^2, are presented in (Table 4).

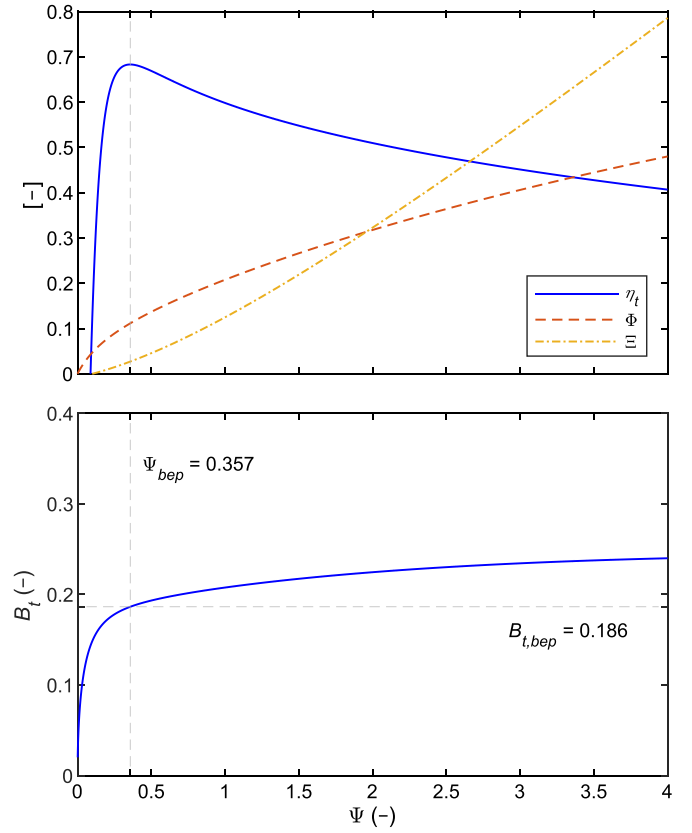It is important to note that in the case of impulse turbines, the

Fig. 9. Efficiency (η_{turb}), dimensionless flow rate (Φ) and dimensionless power (Ξ) as functions of the dimensionless pressure head (Ψ) for a biradial turbine (adapted from (Henriques et al., 2019)) (top); dimensionless damping coefficient of the turbine with the value that corresponds to the best efficiency point ($B_{t,bep}$) marked (bottom).

Table 4
Representative values of the pressure versus flow rate ratio ($\Delta p \, Q^{-2}$), dimensionless damping coefficient of the chamber (B_c) and equivalent full-size biradial turbine diameter (D) for the four tested orifice diameters (d).

d (mm)	$\Delta p \, Q^{-2}$ (kg/m^7)	B_c ($-$)	D (m)
17	2.1×10^7	5.4	1.1
22	7.5×10^6	3.2	1.4
25	4.6×10^6	2.5	1.6
29	2.6×10^6	1.9	1.8

damping that the turbine exerts on the oscillations of the water column is not significantly affected by the rotational speed of the turbine (Falcão and Gato, 2012), which enables this methodology to be applied. If the rotational speed of the turbine influences the damping, using a single orifice—which yields a single damping value—will be inadequate to accurately represent the behaviour of the turbine. Different approaches would be necessary in the case of linear turbines, such as the Wells turbine (Falcão, 2004; Falcão et al., 2014). Furthermore, it should be emphasized that the proposed methodology does not enable the optimization of the geometric characteristics of the turbine (e.g., hub-to-tip ratio or solidity) but rather focuses on selecting the turbine diameter once the turbine has been optimized and its dimensionless performance curves characterized. Additionally, a limitation arises from the simulation of the turbine by means of an orifice, which, while providing a reasonable approximation to the behaviour of a biradial turbine, does not fully replicate the performance of a real controlled turbine.

5. Impact of turbine diameter on the capture-width ratio

Fig. 10 presents the capture-width ratio matrices for the four tested values of turbine-induced damping, each corresponding to a specific turbine diameter. The OWC geometry attains the highest efficiencies for energy periods in the range of 8 s < T_e < 10 s, as shown in each individual capture-width ratio matrix. Importantly, this result is independent of the diameter of the turbine, that is, the resonant frequency of an OWC chamber is not significantly affected by the turbine-induced damping. Therefore, the geometry of the chamber must be designed to achieve near-resonant conditions for the range of energy periods of the sea states that provide the bulk of energy at the location of interest. Additionally, an appropriate chamber design can be achieved for practically any value of turbine-induced damping.

When comparing the different graphs, it is apparent that the turbine-induced damping greatly influences the performance of the OWC. In fact, the capture-width ratio varies up to 100% (or even higher for specific energy bins) depending on the value of the damping coefficient. For instance, for an energy bin with 2 m < H_{m0} < 3 m and 6 s < T_e < 7 s, the capture-width ratio changes from C_{WR} = 20.8% for B_c = 1.89 to C_{WR} = 42.9% for B_c = 5.4. It is important to note that the damping coefficient of the chamber can be adjusted by selecting the appropriate turbine diameter without compromising the performance of the turbine. Specifically, there are multiple turbine diameters that can yield the same damping effect as a given orifice. Among these possible options, the turbine that offers the best performance is the selected one. Therefore, by following the methodology proposed in this work, the turbine is dimensioned to operate at maximum efficiency. Furthermore, when dealing with non-linear turbines, as the biradial turbine, these results are independent of the rotational speed.

The optimum value of the turbine-induced damping varies depending on the sea state: for the lowest significant wave heights (H_{m0} < 2 m), the highest damping (B_c = 5.4) is that which provides the highest values of the capture-width ratio; for sea states with higher wave heights (H_{m0} > 2 m), and especially intermediate and large periods (T_e > 8 s), the second highest damping (B_c = 3.2) is that which leads to the higher efficiencies. In total, the highest capture-width ratio is achieved with the highest damping for 21 sea states and the second highest damping for the remaining 21 sea states. These values of the damping coefficient are provided by biradial turbines of diameter D = 1.1 m and 1.4 m. The lowest values of the damping coefficient, though, can be discarded as do not provide best figures of capture with ratio for any sea state. Thus, two turbine diameters should be retained for further analysis as provide the highest figures of pneumatic energy capture: D = 1.1 m, appropriate for low energetic locations in which the bulk of energy is provided by sea states with low wave heights (H_{m0} < 2 m), and D = 1.4 m, appropriate for mid and high energetic locations in which the bulk of energy is provided by sea states with moderate to high wave heights (H_{m0} > 2 m).

6. Conclusions

In this work, a comprehensive methodology based on physical and numerical modelling, combined with dimensional analysis, was presented and applied to determine the best turbine-chamber configuration for an L-shaped OWC wave energy converter. This methodology is applicable to non-linear turbines, with this work focusing on the novel self-rectifying biradial turbine.

The methodology encompassed several key steps. First, an experimental campaign was conducted to determine the performance of the OWC under a wide range of irregular wave conditions, virtually
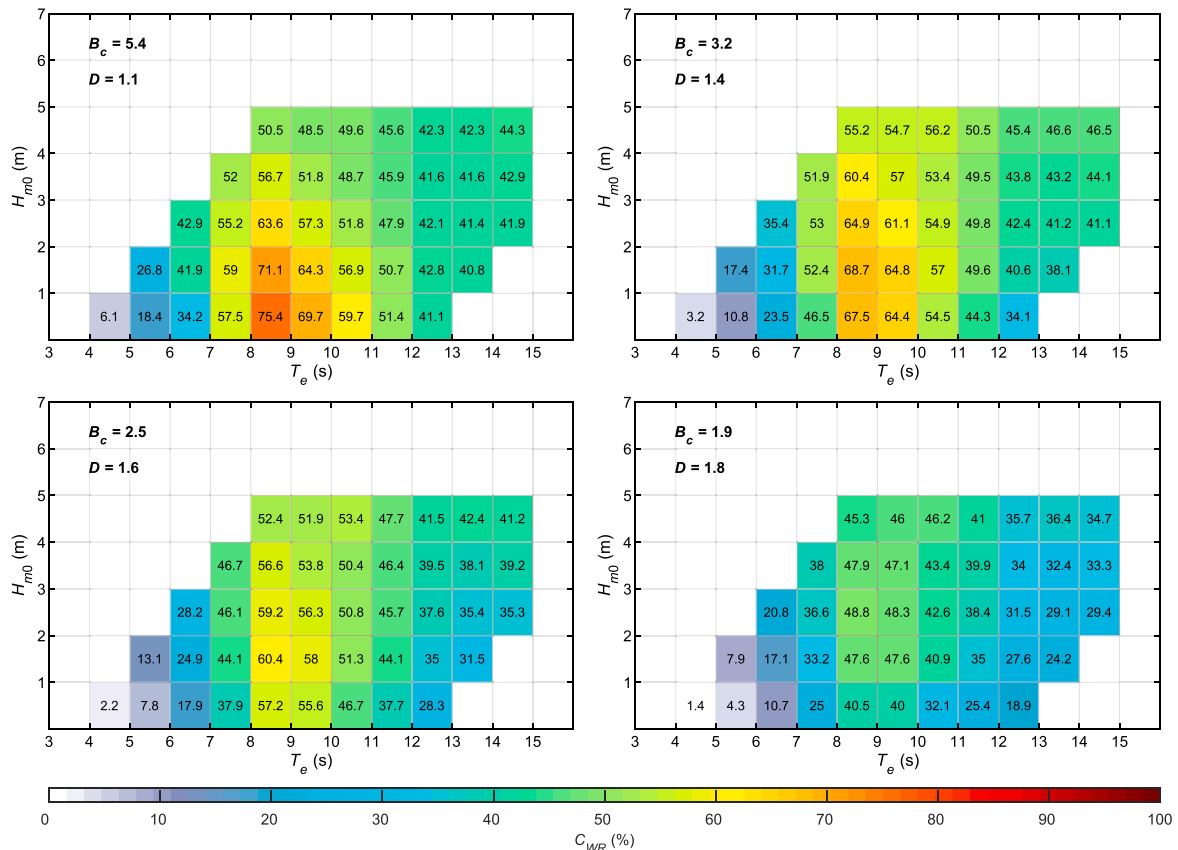

Fig. 10. Capture-width ratio (C_{WR}) matrices of the OWC device for the four tested values of the damping coefficient of the chamber (B_c) and equivalent full-size biradial turbine diameters (D).

comprising the entire range of wave conditions relevant for wave energy exploitation. The campaign considered four values of the turbine-induced damping. Importantly, air compressibility effects, which are typically ignored in small-scale model tests but are known to be significant in full-size OWC devices, were modelled. Second, a numerical model based on the Navier-Stokes equations for two compressible fluids was implemented and validated to determine the pressure versus flow rate relation for the different damping conditions tested. The outputs of both models, physical and numerical, were combined to provide the representative capture-width ratio for each sea state. Finally, dimensional analysis was applied to obtain the diameter of the biradial turbine which provides each one of the four damping conditions tested while operating at maximum performance. On this basis, the capture-width ratio matrices of the OWC were determined for the four turbine diameters.

The results achieved showed that conveniently adjusting the turbine-induced damping by selecting the correct turbine diameter significantly improves capture-width ratio figures, with potential increases of up to 100% for individual sea states. Incidentally, the methodology ensured that the turbines operate at their maximum efficiency for each diameter. Among the four biradial turbine diameters investigated, two diameters ($D = 1.1$ and 1.4 m) were particularly effective in maximizing pneumatic power capture. The smaller diameter ($D = 1.1$ m) should be used for OWC converters at low-energy sites, where the bulk of the energy is provided by sea states with small wave heights ($H_{m0} < 2$ m); conversely, the larger diameter ($D = 1.4$ m) is appropriate for mid- and high-energy sites, where the wave energy resource is provided chiefly by sea states with moderate and large wave heights ($H_{m0} > 2$ m).

The primary contribution of this research lies in the development of a versatile and straightforward methodology applicable to any OWC geometry. Essential inputs for its implementation include: (i) the damping exerted on the water column oscillations; and (ii) the performance characteristic curves of the non-linear turbine of interest. This methodology enables designers to determine the biradial turbine diameter that best matches the air chamber of a given OWC wave energy converter at any site, ensuring maximum performance of both elements, turbine and chamber. Future work will focus on further validation of the proposed methodology, incorporating the efficiency of the turbine-generator set to identify any necessary adjustments.

CRediT authorship contribution statement

I. López: Writing – original draft, Visualization, Validation, Methodology, Investigation, Formal analysis, Conceptualization. **R. Carballo:** Writing – review & editing, Supervision, Project administration, Methodology, Investigation, Funding acquisition, Conceptualization. **D. M. Fouz:** Writing – review & editing, Visualization, Investigation, Formal analysis. **G. Iglesias:** Writing – review & editing, Supervision.

Declaration of competing interest

The authors declare that they have no known competing financial interests or personal relationships that could have appeared to influence the work reported in this paper.

Acknowledgements

References

Astariz, S., Iglesias, G., 2017. The collocation feasibility index–A method for selecting sites for co-located wave and wind farms. Renew. Energy 103, 811–824.

Astariz, S., Iglesias, G., 2016. Selecting optimum locations for co-located wave and wind energy farms. Part II: a case study. Energy Convers. Manag. 122, 599–608.

Astariz, S., Perez-Collazo, C., Abanades, J., Iglesias, G., 2016. Hybrid wave and offshore wind farms: a comparative case study of co-located layouts. Int. J. Mar. Energy 15, 2–16. https://doi.org/10.1016/j.ijome.2016.04.016.

Bao, X., Li, F., Sun, H., Iglesias, G., Shi, H., 2023. Performance characteristics and parameter analysis of a multi-DOF wave energy converter with hybrid power take-off systems. Energy Convers. Manag. 278, 116751 https://doi.org/10.1016/j.enconman.2023.116751.

Boccotti, P., 2007. Comparison between a U-OWC and a conventional OWC. Ocean Eng. 34, 799–805. https://doi.org/10.1016/j.oceaneng.2006.04.005.

Carballo, R., Iglesias, G., 2012. A methodology to determine the power performance of wave energy converters at a particular coastal location. Energy Convers. Manag. 61, 8–18. https://doi.org/10.1016/j.enconman.2012.03.008.

Çelik, A., Altunkaynak, A., 2020. Determination of hydrodynamic parameters of a fixed OWC by performing experimental and numerical free decay tests. Ocean Eng. 204, 106827 https://doi.org/10.1016/j.oceaneng.2019.106827.

Çelik, A., Altunkaynak, A., 2019. Experimental investigations on the performance of a fixed-oscillating water column type wave energy converter. Energy 188. https://doi.org/10.1016/j.energy.2019.116071, 116071–116071.

Çelik, A., Altunkaynak, A., 2018. Experimental and analytical investigation on chamber water surface fluctuations and motion behaviours of water column type wave energy converter. Ocean Eng. 150, 209–220. https://doi.org/10.1016/j.oceaneng.2017.12.065.

Chen, P., Wu, D., 2024. A review of hybrid wave-tidal energy conversion technology. Ocean Eng. 303, 117684 https://doi.org/10.1016/j.oceaneng.2024.117684.

Cui, L., Zheng, S., Zhang, Y., Miles, J., Iglesias, G., 2021. Wave power extraction from a hybrid oscillating water column-oscillating buoy wave energy converter. Renew. Sustain. Energy Rev. 135, 110234 https://doi.org/10.1016/j.rser.2020.110234.

Dick, E., 2015. Fundamentals of Turbomachines. Springer, Netherlands, Dordrecht. https://doi.org/10.1007/978-94-017-9627-9.

Falcão, A.F.O., 2004. Stochastic modelling in wave power-equipment optimization: maximum energy production versus maximum profit. Ocean Eng. 31, 1407–1421. https://doi.org/10.1016/j.oceaneng.2004.03.004.

Falcão, A.F.O., Gato, L.M.C., 2012. 8.05 - air turbines. In: Sayigh, A. (Ed.), Comprehensive Renewable Energy. Elsevier, Oxford, pp. 111–149. https://doi.org/10.1016/B978-0-08-087872-0.00805-2.

Falcão, A.F.O., Gato, L.M.C., Nunes, E.P.A.S., 2013. A novel radial self-rectifying air turbine for use in wave energy converters. Renew. Energy 50, 289–298. https://doi.org/10.1016/j.renene.2012.06.050.

Falcão, A.F.O., Henriques, J.C.C., 2019. The spring-like air compressibility effect in oscillating-water-column wave energy converters: review and analyses. Renew. Sustain. Energy Rev. 112, 483–498. https://doi.org/10.1016/j.rser.2019.04.040.

Falcão, A.F.O., Henriques, J.C.C., 2016. Oscillating-water-column wave energy converters and air turbines: a review. Renew. Energy 85, 1391–1424. https://doi.org/10.1016/j.renene.2015.07.086.

Falcão, A.F.O., Henriques, J.C.C., 2014. Model-prototype similarity of oscillating-water-column wave energy converters. Int. J. Mar. Energy 6, 18–34. https://doi.org/10.1016/j.ijome.2014.05.002.

Falcão, A.F.O., Henriques, J.C.C., Gato, L.M.C., 2018. Self-rectifying air turbines for wave energy conversion: a comparative analysis. Renew. Sustain. Energy Rev. 91, 1231–1241. https://doi.org/10.1016/j.rser.2018.04.019.

Falcão, A.F.O., Henriques, J.C.C., Gato, L.M.C., Gomes, R.P.F., 2014. Air turbine choice and optimization for floating oscillating-water-column wave energy converter. Ocean Eng. 75, 148–156. https://doi.org/10.1016/j.oceaneng.2013.10.019.

Gaspar, L.A., Teixeira, P.R.F., Didier, E., 2020. Numerical analysis of the performance of two onshore oscillating water column wave energy converters at different chamber wall slopes. Ocean Eng. 201 https://doi.org/10.1016/j.oceaneng.2020.107119, 107119–107119.

Gato, L.M.C., Henriques, J.C.C., Carrelhas, A.A.D., 2022. Sea trial results of the biradial and Wells turbines at Mutriku wave power plant. Energy Convers. Manag. 268, 115936 https://doi.org/10.1016/j.enconman.2022.115936.

Hasselmann, D.E., Dunckel, M., Ewing, J.A., 1980. Directional wave spectra observed during JONSWAP 1973. J. Phys. Oceanogr. 10, 1264–1280. https://doi.org/10.1175/1520-0485(1980)010<1264:DWSODJ>2.0.CO;2.

Henriques, J.C.C., Portillo, J.C.C., Sheng, W., Gato, L.M.C., Falcão, A.F.O., 2019. Dynamics and control of air turbines in oscillating-water-column wave energy converters: analyses and case study. Renew. Sustain. Energy Rev. 112, 571–589. https://doi.org/10.1016/j.rser.2019.05.010.

Hirt, C.W., Nichols, B.D., 1981. Volume of fluid (VOF) method for the dynamics of free boundaries. J. Comput. Phys. 39, 201–225. https://doi.org/10.1016/0021-9991(81)90145-5.

Howe, D., Nader, J.R., 2017. OWC WEC integrated within a breakwater versus isolated: experimental and numerical theoretical study. Int. J. Mar. Energy 20, 165–182. https://doi.org/10.1016/j.ijome.2017.07.008.

Hughes, S.A., 1993. Physical Models and Laboratory Techniques in Coastal Engineering. World Scientific, Singapore.

Jacobsen, N.G., Fuhrman, D.R., Fredsøe, J., 2012. A wave generation toolbox for the open-source CFD library: OpenFoam®. Int. J. Numer. Methods Fluid. 70, 1073–1088. https://doi.org/10.1002/fld.2726.

Kim, J.-S., Nam, B.W., Park, S., Kim, K.-H., Shin, S.-H., Hong, K., 2022. Numerical investigation on hydrodynamic energy conversion performance of breakwater-integrated oscillating water column-wave energy converters. Ocean Eng. 253, 111287 https://doi.org/10.1016/j.oceaneng.2022.111287.

Kotb, A.T.M., Nawar, M.A.A., Attai, Y.A., Mohamed, M.H., 2023. Performance optimization of a modified Wells turbine for wave energy conversion. Ocean Eng. 280, 114849 https://doi.org/10.1016/j.oceaneng.2023.114849.

Lamont-Kane, P., Folley, M., Frost, C., Whittaker, T., 2024. Conceptual hydrodynamics of 2 dimensional lift-based wave energy converters. Ocean Eng. 298, 117084 https://doi.org/10.1016/j.oceaneng.2024.117084.

Li, Y., Liu, S., Xu, C., Li, D., Shi, H., 2022. Experimental study on the cylindrical oscillating water column device. Ocean Eng. 246, 110523 https://doi.org/10.1016/j.oceaneng.2022.110523.

Liu, Z., Jin, Y., Cao, L., Liu, G., Guo, H., 2024. Hydrodynamic performance of an oscillating water column integrated into a hybrid monopile foundation. Ocean Eng. 299, 117062 https://doi.org/10.1016/j.oceaneng.2024.117062.

López, I., Carballo, R., Fouz, D.M., Iglesias, G., 2021. Design selection and geometry in OWC wave energy converters for performance. Energies. https://doi.org/10.3390/en14061707.

López, I., Carballo, R., Iglesias, G., 2019. Site-specific wave energy conversion performance of an oscillating water column device. Energy Convers. Manag. 195, 457–465. https://doi.org/10.1016/j.enconman.2019.05.030.

López, I., Carballo, R., Taveira-Pinto, F., Iglesias, G., 2020. Sensitivity of OWC performance to air compressibility. Renew. Energy 145, 1334–1347. https://doi.org/10.1016/j.renene.2019.06.076.

López, I., Pereiras, B., Castro, F., Iglesias, G., 2015. Performance of OWC wave energy converters: influence of turbine damping and tidal variability. Int. J. Energy Res. 39, 472–483. https://doi.org/10.1002/er.3239.

López, I., Pereiras, B., Castro, F., Iglesias, G., 2014. Optimisation of turbine-induced damping for an OWC wave energy converter using a RANS-VOF numerical model. Appl. Energy 127, 105–114. https://doi.org/10.1016/j.apenergy.2014.04.020.

López, M., Ramos, V., Rosa-Santos, P., Taveira-Pinto, F., 2018. Effects of the PTO inclination on the performance of the CECO wave energy converter. Mar. Struct. 61, 452–466. https://doi.org/10.1016/j.marstruc.2018.06.016.

Luo, Y., Presas, A., Wang, Z., 2019. Numerical analysis of the influence of design parameters on the efficiency of an OWC axial impulse turbine for wave energy conversion. Energies 12. https://doi.org/10.3390/en12050939, 939–939.

Martinez, A., Iglesias, G., 2020. Wave exploitability index and wave resource classification. Renew. Sustain. Energy Rev. 134, 110393 https://doi.org/10.1016/j.rser.2020.110393.

Medina-López, E., Moñino, A., Borthwick, A.G.L., Clavero, M., 2017. Thermodynamics of an OWC containing real gas. Energy 135, 709–717. https://doi.org/10.1016/j.energy.2017.06.164.

Medina-López, E., Moñino Ferrando, A., Clavero Gilabert, M., del Pino, C., Losada Rodríguez, M., 2016. Note on a real gas model for OWC performance. Renew. Energy 85, 588–597. https://doi.org/10.1016/j.renene.2015.07.017.

Menter, F.R., Kuntz, M., Langtry, R., 2003. Ten years of industrial experience with the SST turbulence model. Turbul. Heat Mass Tran. 4, 625–632.

Michele, S., Renzi, E., Perez-Collazo, C., Greaves, D., Iglesias, G., 2019. Power extraction in regular and random waves from an OWC in hybrid wind-wave energy systems. Ocean Eng. 191, 106519 https://doi.org/10.1016/j.oceaneng.2019.106519.

Morris-Thomas, M.T., Irvin, R.J., Thiagarajan, K.P., 2007. An investigation into the hydrodynamic efficiency of an oscillating water column. J. Offshore Mech. Arctic Eng. 129, 273–278. https://doi.org/10.1115/1.2426992.

Pereiras, B., Castro, F., el Marjani, A., Rodriguez, M.A., 2011. An improved radial impulse turbine for OWC. Renew. Energy 36, 1477–1484. https://doi.org/10.1016/j.renene.2010.10.013.

Pereiras, B., López, I., Castro, F., Iglesias, G., 2015. Non-dimensional analysis for matching an impulse turbine to an OWC (oscillating water column) with an optimum energy transfer. Energy 87, 481–489. https://doi.org/10.1016/j.energy.2015.05.018.

Perez-Collazo, C., Greaves, D., Iglesias, G., 2018. A novel hybrid wind-wave energy converter for jacket-frame substructures. Energies 11. https://doi.org/10.3390/en11030637.

Pérez-Collazo, C., Greaves, D.M., Iglesias, G., 2023. A jacket-frame mounted oscillating water column with a variable aperture skirt. J. Mar. Sci. Eng. 11 https://doi.org/10.3390/jmse11122383.

Perez-Collazo, C., Pemberton, R., Greaves, D., Iglesias, G., 2019. Monopile-mounted wave energy converter for a hybrid wind-wave system. Energy Convers. Manag. 199, 111971.

Raghunathan, S., 1995. The wells air turbine for wave energy conversion. Prog. Aero. Sci. 31, 335–386. https://doi.org/10.1016/0376-0421(95)00001-F.

Rezanejad, K., Bhattacharjee, J., Guedes Soares, C., 2013. Stepped sea bottom effects on the efficiency of nearshore oscillating water column device. Ocean Eng. 70, 25–38. https://doi.org/10.1016/j.oceaneng.2013.05.029.

Rezanejad, K., Souto-Iglesias, A., Guedes Soares, C., 2019. Experimental investigation on the hydrodynamic performance of an L-shaped duct oscillating water column wave energy converter. Ocean Eng. 173, 388–398. https://doi.org/10.1016/j.oceaneng.2019.01.009.

Sheng, W., Alcorn, R., Lewis, A., 2014. Assessment of primary energy conversions of oscillating water columns. II. Power take-off and validations. J. Renew. Sustain. Energy 6, 053114. https://doi.org/10.1063/1.4896851.

Sheng, W., Alcorn, R., Lewis, A., 2013. On thermodynamics in the primary power conversion of oscillating water column wave energy converters. J. Renew. Sustain. Energy 5, 23105–23105.

Simonetti, I., Cappietti, L., Elsafti, H., Oumeraci, H., 2018. Evaluation of air compressibility effects on the performance of fixed OWC wave energy converters using CFD modelling. Renew. Energy 119, 741–753. https://doi.org/10.1016/j.renene.2017.12.027.

Teixeira, P.R.F., Didier, E., 2023. Numerical analysis of performance of an oscillating water column wave energy converter inserted into a composite breakwater with rubble mound foundation. Ocean Eng. 278, 114421 https://doi.org/10.1016/j.oceaneng.2023.114421.

Vanneste, D., Troch, P., 2015. 2D numerical simulation of large-scale physical model tests of wave interaction with a rubble-mound breakwater. Coast. Eng. 103, 22–41. https://doi.org/10.1016/j.coastaleng.2015.05.008.

Veigas, M., Iglesias, G., 2015. A hybrid wave-wind offshore farm for an island. Int. J. Green Energy 12, 570–576.

Zheng, S., Meylan, M.H., Zhu, G., Greaves, D., Iglesias, G., 2020a. Hydroelastic interaction between water waves and an array of circular floating porous elastic plates. J. Fluid Mech. 900, A20 https://doi.org/10.1017/jfm.2020.508.

Zheng, S., Zhang, Y., Iglesias, G., 2020b. Power capture performance of hybrid wave farms combining different wave energy conversion technologies: the H-factor. Energy 204, 117920. https://doi.org/10.1016/j.energy.2020.117920.

Zheng, S., Zhang, Y., Iglesias, G., 2020c. Concept and performance of a novel wave energy converter: variable Aperture Point-Absorber (VAPA). Renew. Energy 153, 681–700. https://doi.org/10.1016/j.renene.2020.01.134.

Zheng, S., Zhang, Y., Iglesias, G., 2019. Coast/breakwater-integrated OWC: a theoretical model. Mar. Struct. 66, 121–135. https://doi.org/10.1016/j.marstruc.2019.04.001.

Zhou, Y., Ning, D., Chen, L., Iglesias, G., 2021. Nonlinear hydrodynamic modeling of an offshore stationary multi-oscillating water column platform. Ocean Eng. 227, 108919 https://doi.org/10.1016/j.oceaneng.2021.108919.